ADVANCED MATERIALS
www.advmat.de

Nanoengineered Neutrophil as ^{19}F-MRI Tracer for Alert Diagnosis and Severity Assessment of Acute Lung Injury

Sha Li, Lei Zhang, Qiuyi Xu, Meiju Sui, Long Xiao, Daiqin Chen, Zhong-Xing Jiang, Xin Zhou, and Shizhen Chen**

Acute lung injury (ALI) is a severe complication in clinical settings. Alert diagnosis and severity assessment of ALI is pivotal to ensure curative treatment and increase survival rates. However, the development of a precise ALI diagnostic strategy remains a pending task. Here, leveraging neutrophil's inflammation-homing and physiological barrier-navigating capability, a facile strategy is proposed for achieving targeted ^{19}F-MRI detection of ALI based on the nanoengineered neutrophil internalized with perfluorocarbon nanoemulsion (Neu@PFC). The remodeling process poses a negligible impact on the neutrophil's inherent activation and transmigration functions. The migratory behavior of Neu@PFC toward pneumonia is confirmed in vivo using an LPS-induced ALI murine model. Direct intratracheal (*i.t.*) administration contributes to a vast deposition of Neu@PFC within the lung, allowing for real-time ^{19}F-MRI visualization and the potential to predict progressive pneumonia. Furthermore, intravenous (*i.v.*) administration of Neu@PFC enables quantitative assessment of the extent of ALI due to the chemokine-guided neutrophil migration. This study not only provides a pathway to diagnose ALI, but also sheds light on the neutrophil recruitment and activation cues in different tissues and inflammatory conditions, which is a prerequisite for developing potential therapeutic approaches.

1. Introduction

Acute lung injury (ALI) is the cause of respiratory insufficiency and characterized by acute inflammation and the resultant anatomical abnormalities, including alveolar injury, increased endothelial permeability, immune cell infiltration and pulmonary edema. These factors result in severe hypoxemia and progressive dyspnea.[1–3] ALI develops rapidly and often occurs alongside multiple organ dysfunction syndrome due to an uncontrolled inflammatory reaction, which ultimately causes a mortality rate of 20–40%.[4,5] Additionally, ALI-associated respiratory failure is the secondary symptom of advanced coronavirus disease 2019 (COVID-19) infection, which emerged as a significant clinical challenge for the treatment.[6,7] Therefore, exploring a reliable approach for alert diagnosis and severity assessment of ALI during its progression is imperative.[8]

The current clinical diagnosis tools for ALI primarily rely on X-ray and computed tomography (CT).[9–11] However, the findings obtained from these morphological imaging methods often fail to diagnose ALI definitively. Because images show bilateral lung opacities, which can indicate fluid accumulation in the interstitial or alveolar spaces caused by various diseases such as hydrostatic pulmonary edema, diffuse alveolar hemorrhage, acute hypersensitivity pneumonitis, etc.[12,13] As different diseases correspond to different therapeutic regimens, the misdiagnosis of ALI may lead to significant risks to patients. Therefore, developing novel non-invasive imaging techniques that provide early and specific diagnostic information for ALI is necessary.

Magnetic resonance imaging (MRI) is one of the most powerful diagnostic tools in current clinical medicine due to its merits of non-radiation, high resolution, and the ability to provide multi-parameter information. However, the lung represents a problematic territory for traditional ^{1}H-MRI due to sparse proton density and magnetic effects at air/tissue interfaces.[14–16] Over the past years, various strategies have been proposed to enable lung imaging using MRI. ^{19}F is an intrinsically sensitive nucleus for MRI. Endogenous ^{19}F exists in bones and teeth in solid form, undetectable by standard MR techniques. Although ^{19}F is naturally abundant at 100%, it is virtually absent from

S. Li, L. Zhang, Q. Xu, M. Sui, L. Xiao, D. Chen, Z.-X. Jiang, X. Zhou, S. Chen
State Key Laboratory of Magnetic Resonance and Atomic and Molecular Physics
National Center for Magnetic Resonance in Wuhan
Wuhan Institute of Physics and Mathematics
Innovation Academy for Precision Measurement Science and Technology
Chinese Academy of Sciences-Wuhan National Laboratory for Optoelectronics
Huazhong University of Science and Technology
Wuhan 430071, China
E-mail: xinzhou@wipm.ac.cn; chenshizhen@wipm.ac.cn
S. Li, L. Zhang, Q. Xu, M. Sui, L. Xiao, D. Chen, Z.-X. Jiang, X. Zhou, S. Chen
University of Chinese Academy of Sciences
Beijing 100049, China
X. Zhou, S. Chen
School of Biomedical Engineering
Hainan University
Haikou 570228, China

The ORCID identification number(s) for the author(s) of this article can be found under https://doi.org/10.1002/adma.202401513

DOI: 10.1002/adma.202401513

soft tissues. Using exogenous fluorine-containing materials gives rise to "hot spot" ^{19}F-MR image with minimal background noise and a strong signal-to-noise ratio (SNR).[17] The recorded ^{19}F image can be merged with simultaneously acquired and morphologically matched ^{1}H image to locate and observe abnormalities with high specificity.[18–20] It has been demonstrated that several fluorinated gases, such as octafluorocyclobutane, SF_6, perfluoropropane, could be used as contrast agents for lung imaging.[21] Besides, biochemically inert perfluoro-15-crown-5-ether (PFCE) is an alternative ^{19}F-MRI tracer as its 20 chemically and magnetically equivalent fluorine nuclei can provide a single resonance frequency and superior ^{19}F-MRI property.[22,23] It has been reported that emulsified PFCE exhibits selective uptake by the monocyte/macrophage system after systematic appliance in animal models, making it an excellent contrast agent for visualizing the progression of inflammation associated with cardiac and cerebral ischemia.[18,24,25] However, insufficient molecular information about ALI limits precise diagnosis by ^{19}F-MRI, which has prompted research into the design of imaging agents that can facilitate PFCE's targeting of ALI lesion. Wang et al. demonstrated a proof-of-concept study in which alveolar macrophage-mediated translocation of intratracheally delivered PFCE nanoparticles achieved lung cancer ^{19}F-MR imaging.[26] However, the extended metabolic duration of intratracheally administered PFCE in healthy tissue hinders its effectiveness for tumor-specific imaging.

Recently, bioinspired strategies for inflammation-targeted imaging have attracted much attention, with nanoengineered neutrophil emerging as a prominent area of focus.[27] Neutrophils serve as the first line of defense against foreign pathogens and play a crucial role in regulating internal dysfunctions.[28] In the context of ALI, neutrophils are rapidly released from the bone marrow into the bloodstream, resulting in a tenfold increase in circulating neutrophil levels. These boosted neutrophils are subsequently recruited to inflamed lung tissues in response to the release of chemokines such as interleukin-6 (IL-6), interleukin-1β (IL-1β), and tumor necrosis factor-α (TNF-α).[29] Inspired by the chemotactic response of neutrophils to the infection tissue, neutrophil-based cell carriers have been extensively employed to improve the inflammation-targeting capability of nanoparticle-based imaging systems.[30–33] Among the promising methods, both ex vivo labeling and in situ targeting of neutrophils have demonstrated notable potential. Ex vivo approach involves the isolation of neutrophils from the donor's body, which are then modified or loaded with contrast agents in a controlled laboratory environment before being reintroduced into the donor. Compared to in situ targeting strategy, ex vivo manipulation allows for precise control over the labeling process, ensuring consistent and specific modification of neutrophils. For instance, Che et al. demonstrated that neutrophils carrying methotrexate-liposomes retained their physiological activities and migrated to inflamed skeletal muscle and ischemic heart, enhancing the therapeutic effect.[34] Sun et al. reported on using nanoengineered neutrophil loaded with oxygen-carried PFC and sonosensitizer temoporfin for targeted multimodal imaging and treatment of cancer.[35] These studies contribute valuable ideas and methods for neutrophil-mediated PFCE delivery strategy.

In the case of pulmonary diseases, the lung is a unique organ that allows for the direct administration of exogenous imaging agents into the airway via intratracheal (*i.t.*) administration to achieve local delivery.[36] Large available lung surface area, non-invasive and repeatable operation allow rapid diffusion and absorption of imaging agents with enhanced bioavailability and reduced systemic effects.[23,26,37] For the ^{19}F-MRI diagnosis of ALI, the high accumulation of fluorine-containing agents ensures reduced acquisition time and increased signal intensity, providing the feasibility of high contrast and potential alert diagnosis of ALI. However, the uneven deposition of imaging agents within the lung and the difficult delivery to the lower airways by *i.t.* administration pose a challenge to regional MRI quantification of injured lung tissues. In addition, the lungs consist of an extensive blood vessel network for gas exchange and thus can also be reached systematically through the circulation system. Considering the clinical relevance, intravenous (*i.v.*) administration is commonly preferred for most reported diagnostic agents.[37] Through *i.v.* administration, imaging agents reach the bloodstream immediately, providing complete access to the entire body and enabling delivery at a uniform rate. Thus, *i.v.* administration of exogenous fluorine-containing agents may be advantageous for quantitative ^{19}F-MR imaging of regional lung inflammation.

In this study, we have developed nanoengineered neutrophil loaded with perfluorocarbon nanoemulsion (PFC-EM), termed Neu@PFC, for precise ALI diagnosis by ^{19}F-MRI. The biological characteristics of the resultant Neu@PFC were investigated in terms of morphology, cell viability, cell membrane protein markers and in vitro chemotaxis. Neu@PFC maintained the complete functionality of the source neutrophils, which facilitated their investigation with respect to infection infiltration by using lipopolysaccharide (LPS) induced ALI murine model. ^{19}F-MRI and fluorescence imaging techniques were used to compare the pneumonia-targeting and accumulation profile of Neu@PFC with that of bare PFC-EM. *I.t.* administration of Neu@PFC could serve as a screening method to predict progressive pneumonia by ^{19}F-MRI due to the high deposition and selective retention of Neu@PFC in injured lung tissue. Besides, *i.v.* administration of Neu@PFC demonstrated significant efficacy in targeting pneumonia and enabled quantitative measurement of ALI severity. Neu@PFC's infiltration in inflamed lungs after both *i.t.* and *i.v.* administration routes were further confirmed through intravital microscopy (IVM) imaging, with subsequent ex vivo validation by histological and confocal analysis of lung tissues. Taken together, this biomimetic Neu@PFC delivery system is considered a safe, potent and versatile platform for alert diagnosis and severity assessment of ALI by "hot spot" ^{19}F-MRI (**Scheme 1**).

2. Results and Discussion

2.1. Preparation and Characterization of PFC-EM and Neutrophils

The PFC-EM was prepared using a conventional film hydration protocol, and the loading capacity of PFCE was determined to be 10% (wt%). The transmission electron microscopy (TEM) image revealed a spherical structure of PFC-EM with an average diameter of ≈130 nm (**Figure 1a**). Corresponding energy-dispersive X-ray spectroscopy (EDS) element mappings confirmed the homogeneous distribution of carbon, nitrogen, oxygen, and fluorine within the PFC-EM framework, indicating the presence of loaded PFCE (Figure 1b). The mean hydrodynamic diameter of PFC-EM,

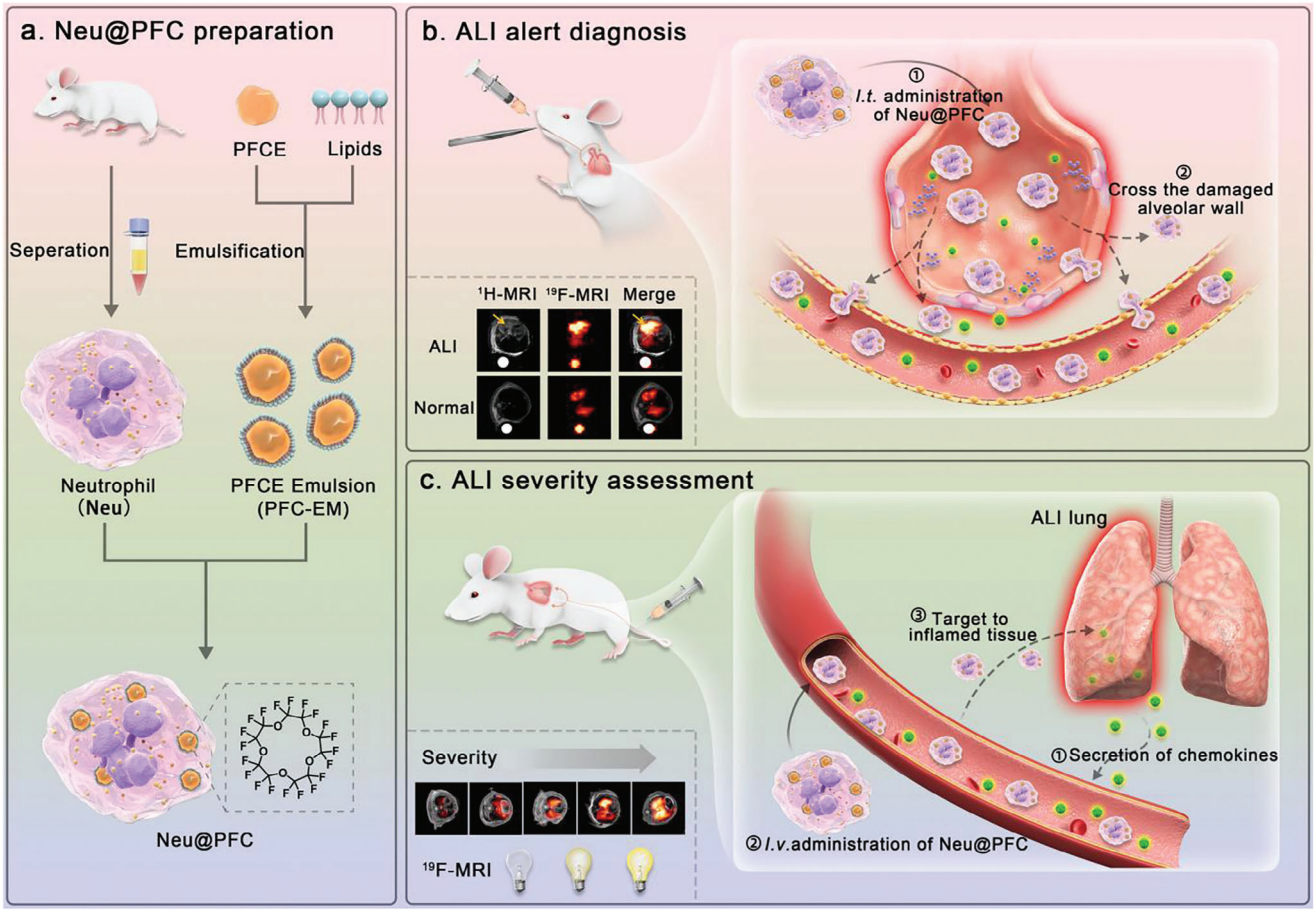

Scheme 1. Schematic illustration of PFC-EM loaded neutrophil (Neu@PFC) for effectively targeting injured lung tissues during ALI through *i.t.* and *i.v.* administration route. a) The nanoengineered Neu@PFC was obtained by incubating the isolated neutrophils with PFC-EM. b) *I.t.* administration ensures a high amount deposition of Neu@PFC within the lung, enabling real-time visualization using ^{19}F-MRI. Combined with the selective retention of Neu@PFC in injured lung tissues, this approach has the potential to serve as a screening method for alert diagnosis of ALI. c) *I.v.* administrated Neu@PFC are guided by inflammatory chemokine gradients in the bloodstream and transmigrate across the vessel wall toward inflamed lungs. This approach provides a quantitative assessment of ALI severity by ^{19}F-MRI.

determined by dynamic light scattering (DLS), was 220 nm with a poly-dispersed index (PDI) of 0.2 (Figure 1c). The ζ-potential of PFC-EM was measured to be +25.7 mV (Figure 1d), which can be attributed to the surface decoration of cationic lipid DOTAP. Notably, the positive charge on the outer surface contributed to the high stability of PFC-EM in an aqueous solution and facilitated its uptake by neutrophils via electrostatic adsorption onto the cell membrane. The ^{19}F-MRI of phantom tubes containing PFC-EM showed a linear correlation between signal intensity and ^{19}F concentration across a range of 6.25–100 mM (Figure 1e,f). This linear relationship indicated that the ^{19}F-MRI signal intensity was solely dependent on the concentration of PFCE, which was beneficial for the in vivo quantification.

Neutrophils were isolated and purified from the peripheral blood of mice using the density-gradient centrifugation method. Wright-Giemsa staining confirmed the successful isolation of neutrophils with typical polymorphic segmented nuclei (Figure 1g). This isolation method yielded a substantial quantity of neutrophils ($\approx 1.5 \times 10^6$ cells mL^{-1} blood), which was essential for the fabrication of nanoengineered neutrophil. The purity of isolated neutrophils was assessed to be 93.9% by using flow cytometry to analyze the expression of characteristic surface markers CD11b and Gr-1 (Figure 1h). The trypan blue staining method was used to document cell death and the viability of neutrophil was determined to be 97.8% (Figure S1, Supporting Information). The mild and fast synthetic procedure employed in the study did not adversely affect the viability of these short-lived cells. The Calcein-AM/PI dual-staining method was used to enumerate viable and nonviable cells. Fluorescent microscopy images and flow cytometric results demonstrated high viability of the neutrophil (Figures 1i and S2, Supporting Information).

2.2. Assembling of Neu@PFC

Neu@PFC were assembled by incubating neutrophils with PFC-EM in the presence of N-formyl-methionyl-leucyl-phenylalanine (fMLP), a potent chemotactic factor that can trigger the phagocytic function of neutrophils (**Figure 2a**). Bio-TEM results confirmed the successful internalization of PFC-EM into neutrophils, validating the assembly of Neu@PFC (Figures 2b and S3, Supporting Information). Scanning electron microscope

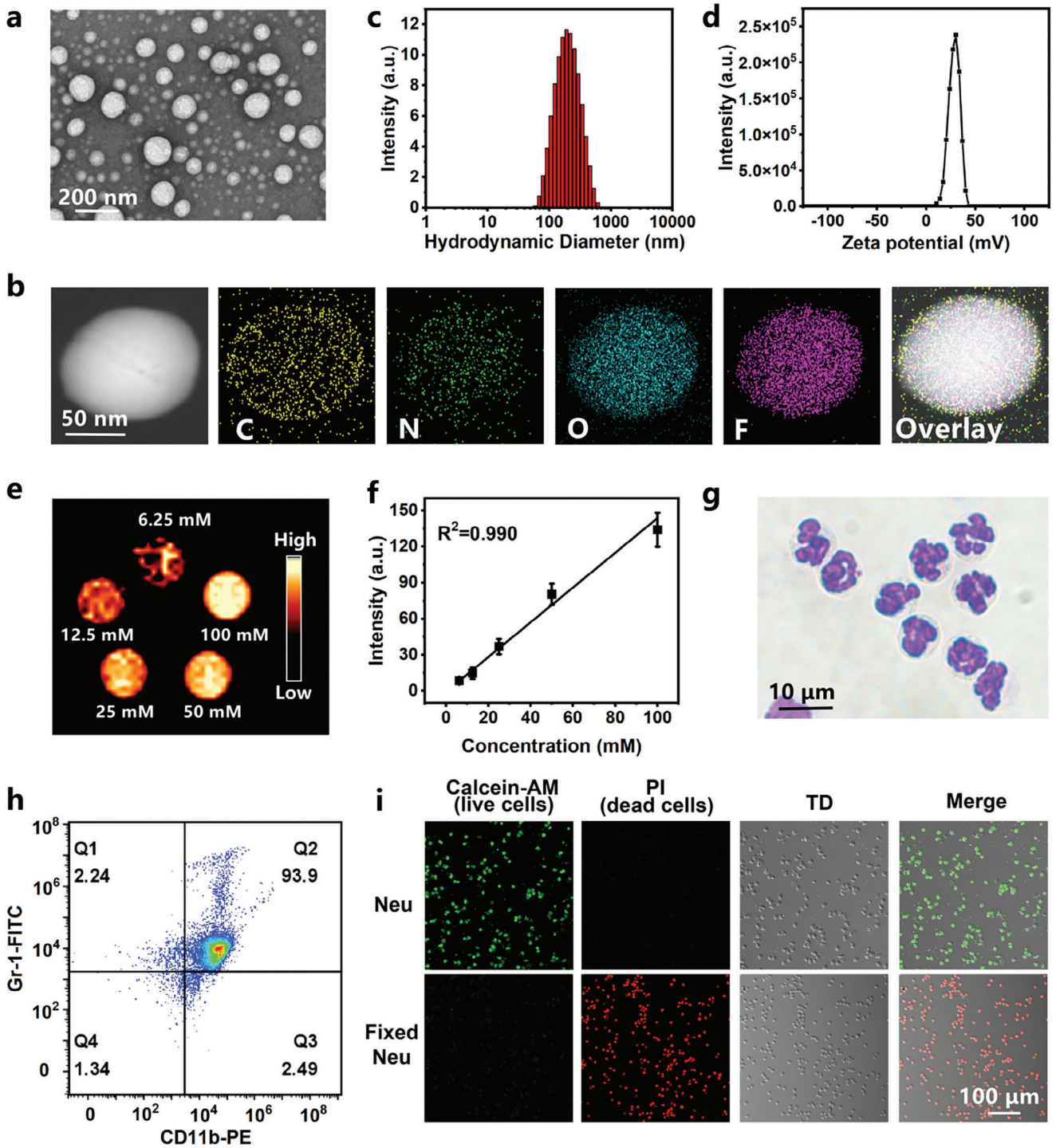

Figure 1. Characterization of PFC-EM and neutrophils. a) TEM image of PFC-EM with negative staining. Scale bar: 200 nm. b) Dark-field TEM image of PFC-EM and corresponding EDS elemental mappings of carbon (C), nitrogen (N), oxygen (O), and fluorine (F). Scale bar: 50 nm. c) Hydrodynamic diameter and (d) ζ-potential of PFC-EM characterized by DLS. e) ^{19}F-MRI phantom images of PFC-EM aqueous solution with various ^{19}F concentrations (6.25, 12.5, 25, 50, 100 mM). Images are axial cross-sections through five NMR tubes. f) The plot of the ^{19}F-MRI signal intensity versus ^{19}F concentration. g) Wright-Giemsa staining of the neutrophils. Scale bar: 10 μm. h) Flow cytometric analysis of the purity of isolated neutrophils by doubly staining with FITC anti-mouse Gr-1 and PE anti-mouse CD11b antibodies. i) Fluorescent microscopy images of Calcein-AM/PI staining of neutrophils and fixed neutrophils. Live cells were stained with calcein-AM (green) and dead cells were labeled with PI (red). Scale bar: 100 μm.

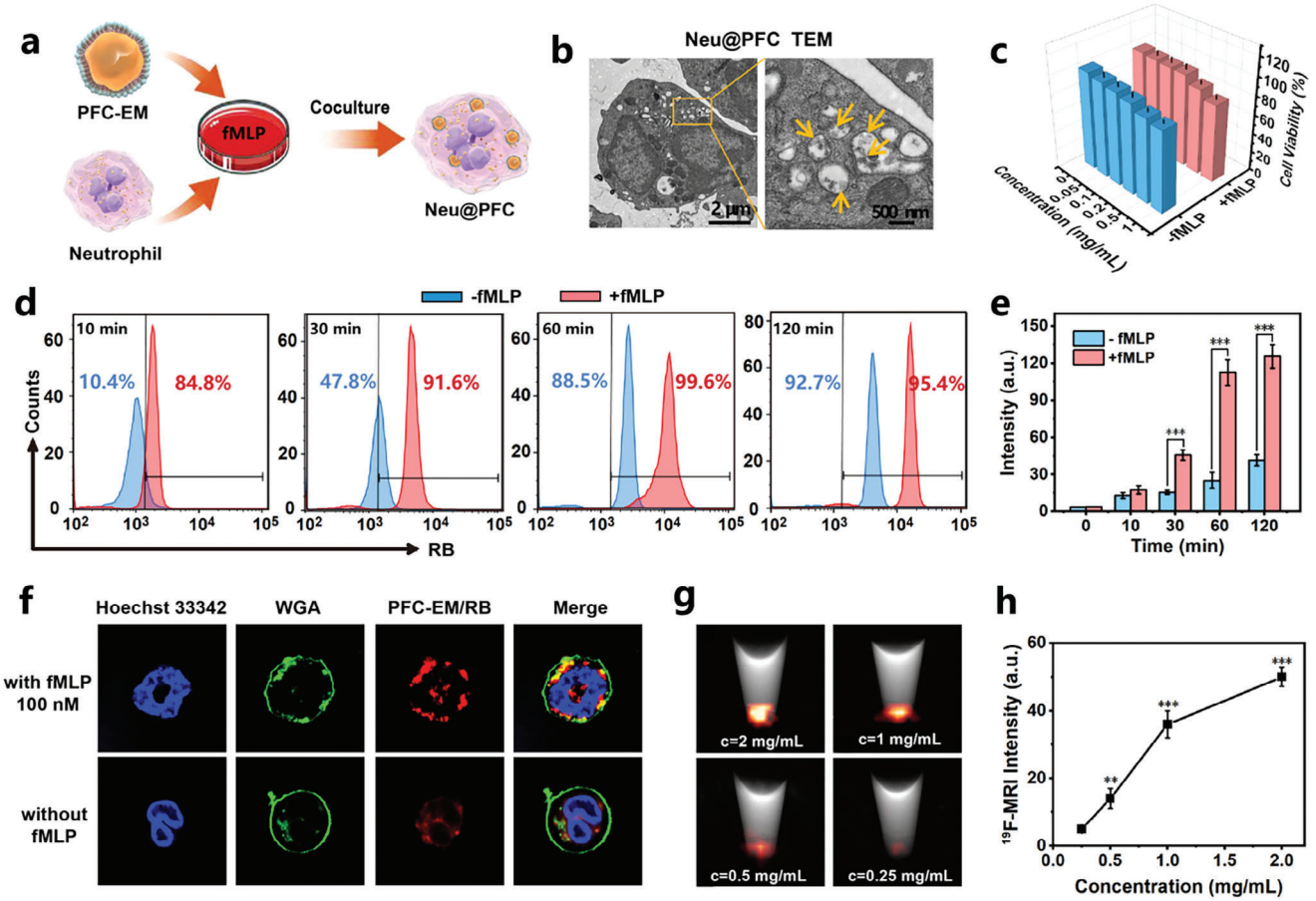

Figure 2. Formulation and characterization of Neu@PFC. a) Schematic illustration of the construction of Neu@PFC by incubating neutrophils with PFC-EM under fMLP activation. b) Bio-TEM images of Neu@PFC. The yellow arrow indicates PFC-EM that neutrophils have internalized via endocytosis. Scale bar: 2 μm. c) Cell viability of neutrophils after coincubation with different concentrations of PFC-EM (0.05, 0.1, 0.2, 0.5, 1 mg mL^{-1}) for 1 h in the presence/absence of fMLP (100 nM). d) Flow cytometry and (e) quantitative determination of cellular uptake efficiency. Neutrophils were incubated with PFC-EM/RB for different times (10, 30, 60, 120 min) with/without fMLP activation. (Mean ± S.D., $n = 3$. Student's t-test, $^{***}p < 0.005$, verified by one-way ANOVA). f) CLSM images of neutrophils incubated with PFC-EM/RB in the presence/absence of fMLP for 1 h. Cell nuclei were stained with Hoechst33342 (blue), and cell membranes were stained with iFluor 488-WGA (green). g) ^{1}H-MRI of microcentrifuge tube merges with ^{19}F-MRI of neutrophils pellets after coincubation with different concentrations (0.25, 0.5, 1, 2 mg mL^{-1}) of PFC-EM. h) Quantification of the ^{19}F-MRI signal intensity of (g). (Mean ± S.D., $n = 3$. Student's t-test, $^{**}p < 0.01$, $^{***}p < 0.005$ versus 0.25 mg mL^{-1} group, verified by one-way ANOVA).

(SEM) images also illustrated an interaction between the positively charged PFC-EM and the negatively charged cell membrane (Figure S4, Supporting Information). The viability of neutrophil after uptake of cargo particles is essential for their role as hitchhiking vehicles. The cytotoxicity of neutrophil after incubation with various concentrations of PFC-EM was assessed using the cell counting kit-8 (CCK-8) assay. The results showed that neutrophils maintained reasonable viability (≥80%) even at PFC-EM coincubation concentrations up to 1 mg mL^{-1} (Figure 2c). The relatively high biocompatibility of PFC-EM can be attributed to the safe excipients used in the formulation.[38]

Rhodamine-B (RB) was labeled on PFC-EM to allow the evaluation of in vitro cellular uptake. Neutrophils were incubated with PFC-EM/RB under both fMLP-free and fMLP-containing conditions at different times. The flow cytometry assay revealed that, in the presence of fMLP, ≈84.8% of neutrophils exhibited intracellular fluorescence after 10 min of incubation, indicating a swift internalization of PFC-EM/RB. In contrast, only 10.4% of neutrophils showed PFC-EM/RB labeling in the absence of fMLP (Figure 2d). The labeling efficacy of PFC-EM/RB in neutrophils further increased after 1 h of incubation and remained relatively stable for the subsequent 2 h under both conditions. Moreover, the fluorescence intensity of intracellular PFC-EM/RB was consistently stronger with fMLP treatment compared to without fMLP treatment at all time points, thereby demonstrating the enhanced efficacy of the proposed neutrophils labeling strategy through fMLP activation (Figures 2e and S6, Supporting Information). Extended incubation time could decrease PFC-EM/RB labeling levels due to neutrophils' immunomodulatory and efflux effects (Figure S5, Supporting Information). To ensure optimal cellular uptake, 1-h treatment of neutrophils with PFC-EM was employed in the following studies.

The intracellular location of PFC-EM/RB was examined using confocal laser scanning microscopy (CLSM). The cell membrane was stained with iFluor 488-WGA. As shown in Figures 2f and S7 (Supporting Information), most PFC-EM/RB existed in

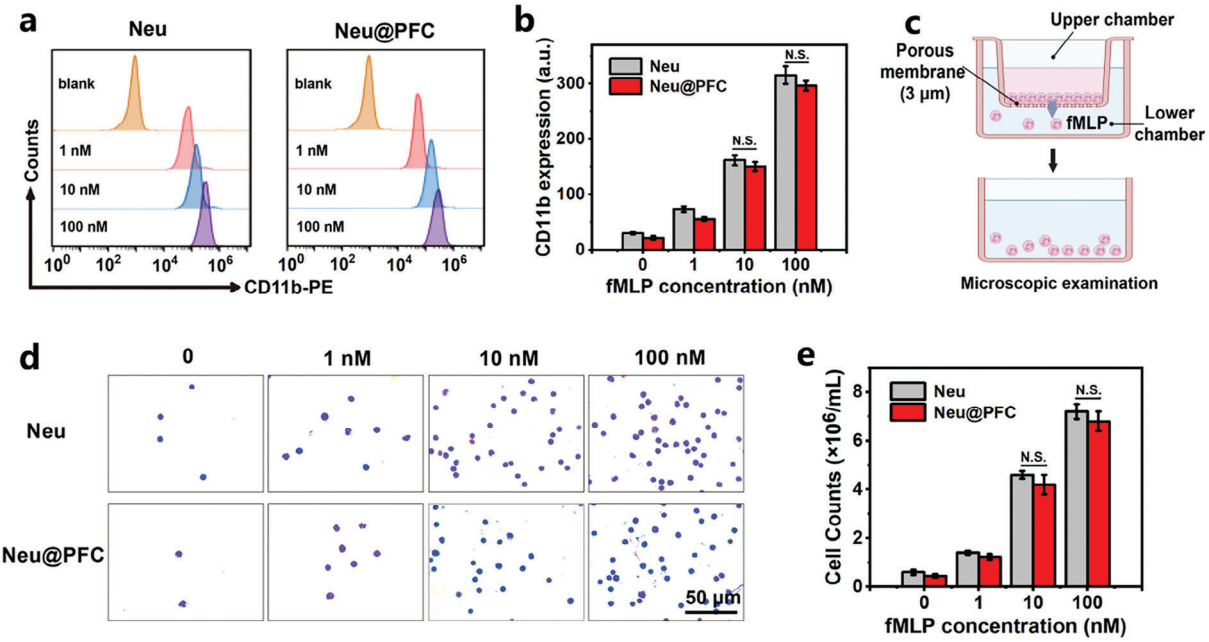

Figure 3. In vitro chemotaxis capability of Neu@PFC. a) Flow cytometry and b) quantitative determination of expression level of CD11b on neutrophils and Neu@PFC after treatment with different concentrations of fMLP (1, 10, and 100 nM) for 30 min. CD11b was stained with PE anti-mouse CD11b antibody. (Mean ± S.D., $n = 3$. Student's t-test, N.S.: no significance, verified by one-way ANOVA). c) Schematic illustration of the in vitro model to evaluate the chemotaxis-guided migration capability of neutrophils and Neu@PFC across the porous membrane using a transwell assay. d) Neutrophils and Neu@PFC were stained with crystal violet on the lower chamber and imaged under a microscope. Scale bar: 50 μm. e) Number of migrated neutrophils and Neu@PFC on the lower chamber. (Mean ± S.D., $n = 3$. Student's t-test, N.S.: no significance, verified by one-way ANOVA).

an aggregated form near the nucleus and scattered throughout the cytoplasm of neutrophils. Furthermore, a more rapid and potent uptake of PFC-EM/RB by neutrophils was observed under the fMLP-stimulated condition compared to the unstimulated condition. As shown in Figure S8 (Supporting Information), the red fluorescence of PFC-EM/RB showed colocalization with the green fluorescence of the lysosome probe. This suggested that PFC-EM/RB likely enters neutrophils through an endocytosis mechanism following its initial attachment to the cell membrane.

In vitro ^{19}F-MRI of neutrophils was conducted by incubating them with various concentrations of PFC-EM (0.25 to 2 mg mL^{-1}) for 1 h. The results shown in Figure 2g demonstrated that the neutrophil pellets labeled with PFC-EM were visible on ^{19}F-MRI as a homogeneous "hot spot" region. The signal intensity of the cell pellets increased with higher concentrations of PFC-EM, indicating a dose-dependent internalization behavior of PFC-EM by neutrophils (Figure 2h). Moreover, the loading capacity of PFCE in Neu@PFC was determined using ^{19}F-NMR spectroscopy and found to be as high as 1.75×10^{-4} mmol per 10^6 cells (Figure S9, Supporting Information). These findings highlight the promising potential of Neu@PFC as a "hot spot" ^{19}F-MRI tracer.

2.3. Physiological Functions of Neu@PFC In Vitro

It is believed that the mobilization of neutrophils from blood circulation to inflamed lung tissue is associated with their intravascular motion and chemotactic behavior. Here, the activation state and transmigration function of the neutrophils before and after PFC-EM assembling were systematically studied. Wright-Giemsa staining of Neu@PFC showed that the endocytosis of PFC-EM did not induce membrane roughness or rupture in neutrophils (Figure S10, Supporting Information). CD11b is a member of β-integrin adhesion proteins that critically regulates the adhesion and migration of neutrophils to infection sites. It is upregulated on the occurrence of infection. As anticipated, flow cytometry results demonstrated a notable increase in both the CD11b expression levels of neutrophils and Neu@PFC as the concentration of fMLP increased, and there was no substantial differences among them (**Figure** 3a,b).

Furthermore, the chemotaxis-guided transmigration function of engineered neutrophil was investigated using a transwell plate with a pore size of 3 μm. This system allowed for the exchange of cytokines while preventing the passage of whole cells through the chamber. As shown in Figure 3c, various concentrations of fMLP were placed beneath the chamber, while blank neutrophils or Neu@PFC were seeded into the apical chamber. The transwell membrane hindered the passage of neutrophils when the basolateral side was immersed in fresh media without fMLP. In contrast, the number of migrating neutrophils significantly increased upon adding fMLP, and the migrating number was observed to be dependent on the concentration of fMLP (Figure 3d,e). This finding highlighted the activation of neutrophils' chemotactic function by chemokines. Meanwhile, Neu@PFC behaved similarly to that of unlabeled neutrophils. These results demonstrated that Neu@PFC maintained the physiological functions of neutrophils, enabling a rapid response to inflammatory stimuli and directional migration toward sites of inflammation.

To comprehensively investigate the impacts of PFC-EM and fMLP on neutrophils' effector functions, transcriptome gene expression analysis was performed. A correlation heatmap (Figure S11a, Supporting Information) revealed samples of neutrophils incubated with PFC-EM tightly clustered with that of incubated with PBS, but distinctly separated from that of incubated with fMLP. A comprehensive portrayal of differentially expressed genes (DEGs; Figure S11b, Supporting Information) highlighted thousands of upregulated and downregulated genes in the fMLP group compared with the blank group, while only a few DEGs were found in the PFC-EM group. Furthermore, Gene Ontology (GO) analysis (Figure S11c, Supporting Information) unveiled upregulated DEGs in the fMLP group significantly enriched in a series of chemotaxis-related and inflammation-related pathways. The representative DEGs of inflammatory response and neutrophil chemotaxis pathways were displayed in Figure S11d (Supporting Information). These results indicated a limited impact of neutrophils by PFC-EM incubation and robust activation by fMLP.

2.4. ALI alert Diagnosis by 19F-MRI after *i.t.* Administration of Neu@PFC

The successful in vitro assembly of Neu@PFC and the unaffected chemotactic and transmigration function provided an impetus for the subsequent in vivo targeting assessment in the context of pneumonia. The ALI murine model was established by *i.t. the* instillation of LPS. As an intrinsic component and surface antigen of gram-negative bacteria, LPS instigates a robust proinflammatory response and triggers the release of cytokines such as IL-6, IL-1β, and TNF-α, providing a chemokine gradient conducive to the activation and recruitment of neutrophils (Figures S12 and S13, Supporting Information). CT scans were also used to validate the presence of pulmonary edema in ALI mice (Figures S14 and S15, Supporting Information). The immune response of Neu@PFC on both healthy mice and those with ALI was further evaluated. Following adoptive infusion, the complete blood counts and inflammatory factors (IL-6, IL-1β and TNF-α) in serum and bronchoalveolar lavage fluid (BALF) indicated no significant changes compared to the PBS-treated mice (Figures S16 and S17, Supporting Information). This lack of response may be attributed to the genetic homogeneity and immune tolerance of the isolated neutrophils, which reduces the likelihood of an immune reaction.[39]

The pulmonary delivery strategy should be prioritized when studying lung injury due to its unique advantages of no first-pass effect and high bioavailability. The inflammation-homing effects of Neu@PFC were evaluated on healthy and ALI mice (6 μg g^{-1} LPS instillation) via *i.t.* administration according to the treatment plan outlined in **Figure 4a**. PFC-EM was labeled with the fluorescent dye DiD to prepare PFC-EM/DiD and Neu@PFC/DiD for intuitive observation. Strong fluorescence signals were observed in the lungs at 1 h after administration among all groups (pneumonia mice/Neu@PFC/DiD, pneumonia mice/PFC-EM/DiD, healthy mice/Neu@PFC/DiD) and lasted for up to 48 h (Figure 4b). The main organs were then harvested and imaged subsequently. As shown in Figure 4c, vigorous fluorescence intensity was exclusively observed in the lungs in all groups, with no detection identified in the liver, spleen and intestine, indicating excellent availability for lung imaging. Furthermore, the inflammation status of the lung on histological level was assessed (Figure 4d). Hematoxylin and eosin (H&E) staining of lung tissues displayed notable thickening of the alveolar walls and destruction of the alveolar cavities in ALI mice. Moreover, the lung tissues of the pneumonia mice-Neu@PFC group exhibited enhanced green fluorescence indicative of DiO-labeled neutrophils and red fluorescence corresponding to DiD-labeled PFC-EM. Conversely, weak fluorescence was observed in the lung tissues of control groups. These suggested the elevated infiltration of Neu@PFC in the injured lung tissue.

Next, pulmonary T_2-weighted ^{1}H and density-weighted ^{19}F MR imaging experiments were performed on ALI mice using Neu@PFC with the *i.t.* administration protocol (Figure 4e). Prominent ^{19}F signals were visually observed in the lungs of all groups 1 h post-administration. In the pneumonia mice/Neu@PFC group, the ^{19}F-MR signal intensity of the left lung was more robust compared to the right lung during the 8–24-h period, which was in accordance with the infiltration kinetics of neutrophils toward inflammation reported previously.[40] Presumably, Neu@PFC remained in the inflamed lungs of ALI mice for an extended duration with a delayed fading rate compared to its presence in the healthy lungs of control mice, which can be attributed to the pathological changes of lung inflammation. Furthermore, the quantitative analysis uncovered distinct retention behaviors of *i.t.* administrated Neu@PFC in the lungs of ALI mice (Figure 4f).

T_2-weighted ^{1}H-MRI of ALI mice revealed a hyperintense signal in the left lung region until 24 h post-administration. The intensified ^{19}F-MRI signal in the left lung closely mirrored the marked hyperintense region in ^{1}H-MRI, thereby demonstrating the selective inflammation retention of Neu@PFC. Conversely, PFC-EM did not exhibit selectivity toward injured lung tissue. Notably, lung inflammation may facilitate the homing of Neu@PFC, and the produced ^{19}F-MRI signal preceded the colocalized hyperintense region in the ^{1}H-MRI image. Thus, *i.t.* administration of Neu@PFC could serve as a proper screening method for predicting progressive pneumonia using ^{19}F-MRI.

To demonstrate the intravascular motion of Neu@PFC in the alveolar after *i.t.* administration, intravital microscopy (IVM) imaging of the lung was further carried out. Purified neutrophils were stained with DiO, while PFC-EM were stained with Rhodamine-B to prepare double fluorescent labeled Neu/DiO@PFC/RB. As shown in Figure 4h, neutrophils were primarily located in the alveoli following *i.t.* administration in healthy mice. This was mainly due to the intact alveolar-capillary membranes and the absence of chemotaxis gradient. In pneumonia mice, neutrophils could traverse the damaged alveolar-capillary barrier as hitchhiking cellular vehicles and enter the systemic circulation. As a result, they carried PFC-EM to accumulate in the inflamed lung tissues.

2.5. ALI Severity Measurement by 19F-MRI after *i.v.* Administration of Neu@PFC

ALI is a severe clinical condition characterized by a rising incidence, high mortality rate, and limited effective treatment

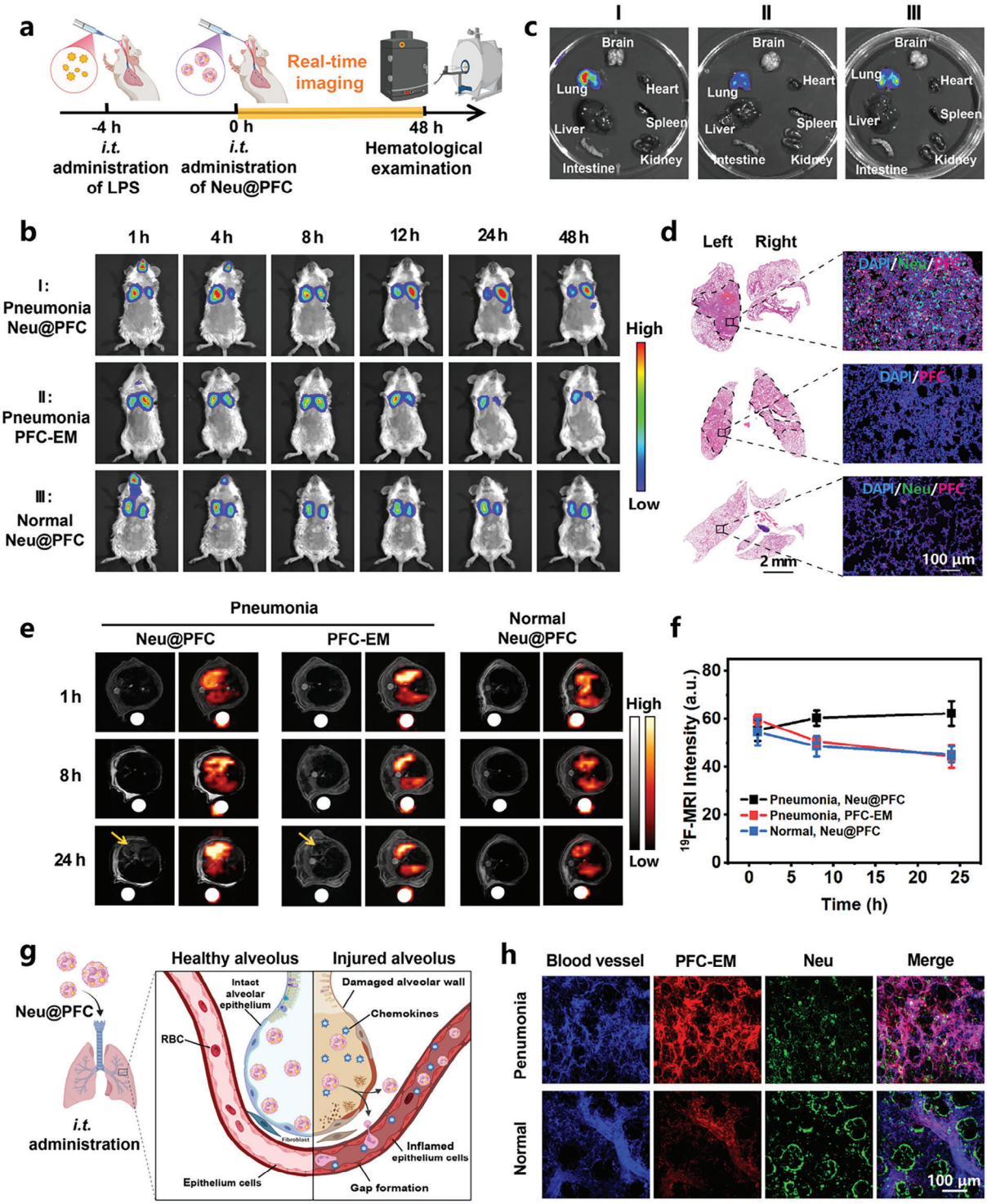

Figure 4. In vivo fluorescence and ^{19}F-MRI of Neu@PFC in ALI mice after *i.t.* administration. a) Schematic time course of establishment of ALI murine model and treatment regimen. b) In vivo optical fluorescence images after *i.t.* administration of Neu@PFC/DiD and PFC-EM/DiD at different times. c) Ex vivo fluorescence images of dissected main organs (brain, heart, liver, spleen, lungs, kidneys, and intestine). d) H&E and confocal images of lung tissue sections treated with Neu@PFC and PFC-EM. Staining depicts DiO labeled Neu (green), DiD labeled PFC-EM (red), and DAPI stained nucleus (blue). The scale bar for the H&E image is 2 mm, and the confocal image is 100 μm. e) In vivo pulmonary T_2-weighted ^{1}H-MRI and density-weighted ^{19}F-MRI after *i.t.* administration of Neu@PFC and PFC-EM at different times. A "hot iron" color lookup table was applied to ^{19}F images. The yellow arrow points to the pulmonary edema area in the ^{1}H-MRI images. f) ^{19}F-MRI signal intensity of lungs versus times. (Mean ± S.D., $n = 3$). g) Schematic illustration of Neu@PFC passing through injured lung alveolus. h) IVM lung imaging of each group. Staining depicts DiO labeled Neu (green), Rhodamine-B labeled PFC-EM (red), and Evance blue labeled vasculature (blue). Scale bar: 100 μm.

options. The impact of ALI on patients' quality of life underscores the urgent need for selective diagnostic strategies to assess its severity and enable timely intervention. In this regard, the *i.t.* administration of Neu@PFC has successfully been used to provide a significant ^{19}F-MRI signal within injured lung tissue. However, the inhomogeneous deposition of Neu@PFC within lung lobes caused by individual respiratory variations limited its further utilization for localized ^{19}F-MRI quantification. Neutrophils migrate to infection sites via chemotaxis from the bloodstream, so we hypothesized that the *i.v.* administration route may improve the selective accumulation of Neu@PFC in the inflamed lung area, making it possible for the severity assessment of ALI.

To validate the precise targeting capability of Neu@PFC for ALI lesion and assess the extent of lung injury, model mice with varying degrees of ALI (0-6 μg g^{-1} LPS instillation) were employed for detection purposes. Neu@PFC/DiD and PFC-EM/DiD were *i.v.* administered to both healthy and ALI mice according to the specified treatment regimen (**Figure** 5a). At 12 h post-administration, the main organs from each group were dissected for ex vivo fluorescence imaging and further confirmed by a quantitative region of interest (ROI) analysis. As shown in Figure 5b,c, in healthy mice, there was a large amount of Neu@PFC/DiD enrichment in the spleen and liver. Meanwhile, in pneumonia mice, Neu@PFC/DiD exhibited significant fluorescence in the lung. Moreover, the severity of ALI correlated with higher fluorescence enrichment. The enhanced targeting of Neu@PFC/DiD to inflamed lungs is likely attributed to the upregulated expression levels of inflammatory cytokines and increased permeability of alveolar capillaries, which is beneficial for neutrophil recruitment (Figure S13, Supporting Information). By contrast, PFC-EM/DiD showed fairly minimal lung accumulation but maintained strong fluorescence in the liver in both healthy and pneumonia mice, which can be attributed to the unselective uptake of PFC-EM/DiD by mononuclear phagocyte system (MPS). Accordingly, neutrophils hitchhiked with PFC-EM can function as an inflammation-guided stealth platform for targeted ALI imaging through *i.v.* administration.

Given the demonstrated tropism of nanoengineered neutrophil for lung inflammation, we sought to investigate the potential of using Neu@PFC as a ^{19}F-MRI tracer for severity assessment on ALI. A representative example of T_2-weighted ^{1}H-MR and density-weighted ^{19}F-MR images obtained 12 h post *i.v.* administration of Neu@PFC and PFC-EM were shown in Figure 5d. The anatomical ^{1}H-MR images provided no evidence of lung alteration after LPS instillation. This is primarily due to the lack of visibility of signals from free protons (e.g., blood vessels), which hinders a more specific identification of evolving hyperintense regions associated with pulmonary edema. In contrast, the corresponding ^{19}F-MR images unambiguously exhibited notable contrast enhancement in the lungs of ALI mice *i.v.* administered with Neu@PFC. The intensity of the ^{19}F-MRI signal showed a strong correlation with the applied LPS dose across a broad concentration range (0.08 to 6 μg g^{-1}). Specifically, the average ^{19}F-MRI intensity of LPS-6 μg g^{-1} stimulated lungs after *i.v.* administration of Neu@PFC showed 1.2, 1.9, 2.7, 8.8-fold enhancements compared to the LPS-1.6, LPS-0.4, LPS-0.08 μg g^{-1}, LPS-0 groups, respectively (Figure 5e). In stark contrast, PFC-EM-administered lungs only showed minimal ^{19}F-MRI signals in ALI mice with high doses of LPS instillation. This limited signal is attributed to the innate neutrophil hitchhiking effects that facilitate PFC-EM to accumulate in inflamed lung tissue. Considering that Neu@PFC can effectively target inflammation through *i.v.* administration, the resulting ^{19}F-MRI image provides a detailed visualization of neutrophils' infiltration toward lung inflammation and quantitative analysis of the ^{19}F-MRI signal in regional tissue.

Lung tissue sections were further assessed by H&E staining and confocal imaging. Figure 5f demonstrated the presence of severe lung injury in LPS-induced ALI mice, characterized by pulmonary edema and alveolar wall thickening. Furthermore, the lung tissue exhibited an accumulation pattern of Neu@PFC toward ALI similar to that observed in ex vivo fluorescence imaging and ^{19}F-MRI results. Additional IVM lung imaging also confirmed the extensive infiltration of Neu@PFC in the microcirculation of the pulmonary injury region compared to bare PFC-EM (Figure S18, Supporting Information). These findings indicate that the unique properties of neutrophils, namely their ability to traverse blood vessel barriers and move toward inflammation sites, contribute to the substantial accumulation of PFC-EM in ALI. This approach proves to be a powerful method for accurately measuring the severity of lung injury.

2.6. Safety Evaluation of Neu@PFC

To evaluate the in vivo biological safety of Neu@PFC and PFC-EM, a comprehensive analysis of the blood routine and biochemical indexes assay were performed on healthy mice 24 h post *i.v.* and *i.t.* administration, respectively. Compared with mice administered with PBS, there was no significant difference in counts of blood cells (Figures S19 and S20, Supporting Information). Moreover, the blood expression levels of aspartate aminotransferase (AST), alanine aminotransferase (ALT), alkaline phosphatase (ALP), creatinine (Cre), and blood urea nitrogen (BUN) of mice were sustained in the normal range, suggesting no hepatic or renal dysfunction. The heart, liver, spleen, lungs, and kidneys were also processed by H&E staining. The overall structural integrity of all the tissues was nearly identical to those from mice administered with PBS, demonstrating no signs of acute toxicity and further supporting the safety of Neu@PFC and PFC-EM through both *i.v.* and *i.t.* administration. Collectively, these data revealed the excellent biocompatibility and negligible side effects of the Neu@PFC.

3. Conclusion

In summary, we have shown that neutrophil with intrinsic chemotaxis capability can be engineered into self-guided biohybrid ^{19}F-MRI tracer by integrating synthesized perfluorocarbon nanoparticles (Neu@PFC) for alert diagnosis and severity assessment of ALI. This fabrication process of Neu@PFC exhibits high fluorine loading efficiency with negligible influence on the biological profiles of host neutrophils in terms of morphology, cell viability, cell surface protein markers and in vitro chemotaxis. Compared with bare PFC-EM in an LPS-induced ALI murine model, Neu@PFC showed a faster targeting effect and more robust accumulation for pneumonia through multi-route delivery, as revealed by ^{19}F-MRI and fluorescence imaging. On the one hand,

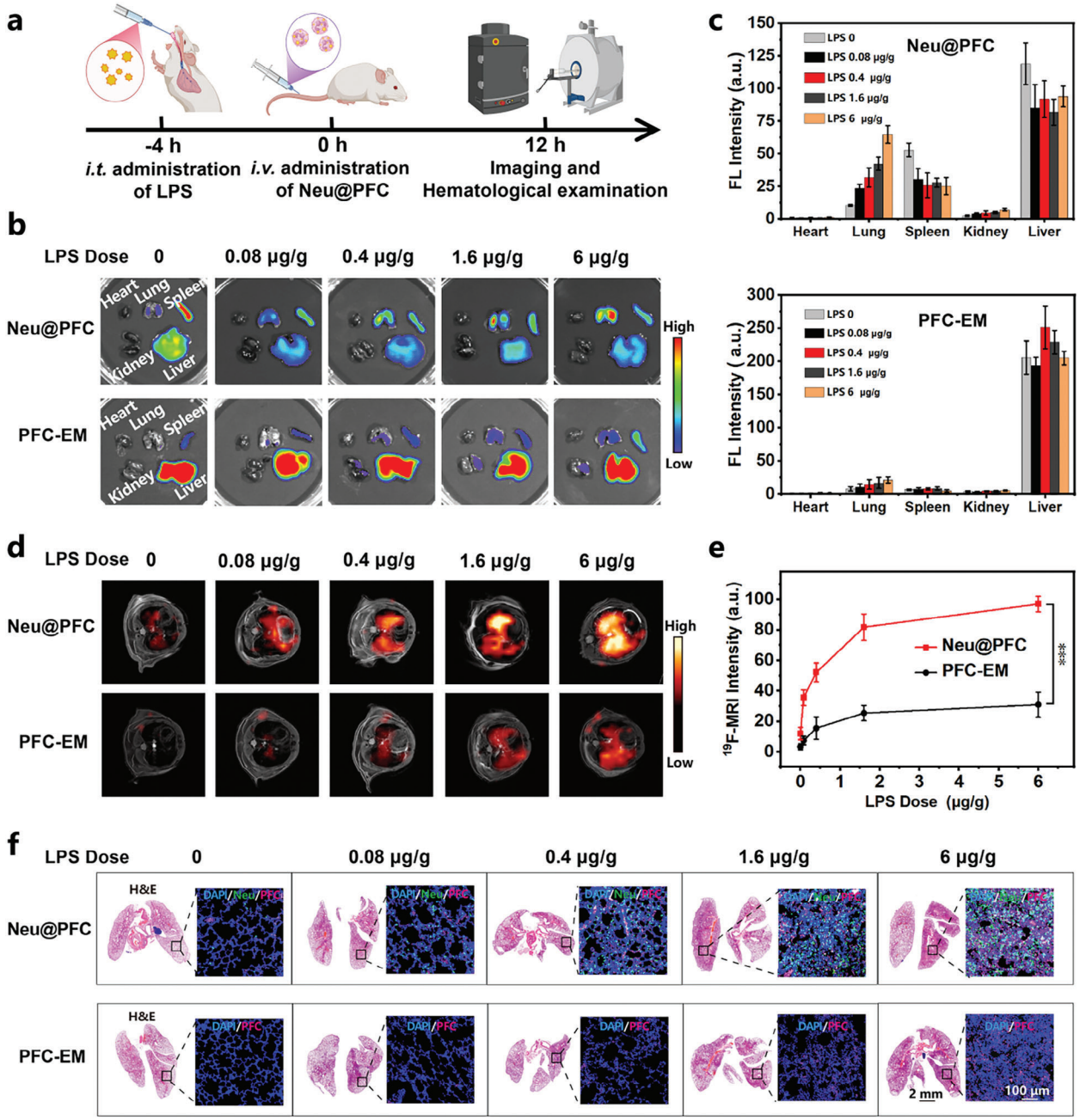

Figure 5. Ex vivo fluorescence biodistribution and in vivo ^{19}F-MRI of Neu@PFC in ALI mice after *i.v.* administration. a) Schematic time course of establishment of ALI murine model and treatment regimen. b) Ex vivo fluorescence images of dissected organs (heart, liver, spleen, lungs, kidneys) 12 h post *i.v.* administration of Neu@PFC/DiD and PFC-EM/DiD to ALI mice with varying concentrations of LPS instillation (0, 0.08, 0.4, 1.6, and 6 μg g^{-1}). c) Fluorescence quantification of major organs in different groups. (Mean ± S.D., $n = 3$). d) T_2-weighted ^{1}H-MRI and density-weighted ^{19}F-MRI of mice after *i.v.* administration of Neu@PFC and PFC-EM. A "hot iron" color lookup table was applied to ^{19}F images. e) ^{19}F-MRI signal intensity of lungs in different groups. (Mean ± S.D., $n = 3$. Student's *t*-test, $^{***}p < 0.005$, verified by one-way ANOVA). f) H&E and confocal images of lung tissues of different groups. Staining depicts DiO-labeled neutrophils (green), DiD-labeled PFC-EM (red), and DAPI-stained nucleus (blue). The scale bar for the H&E image is 2 mm, and the confocal image is 100 μm.

i.t. administration facilitated direct deposition of Neu@PFC into the lung. The selective retention of Neu@PFC in injured lung tissue, coupled with real-time ^{19}F-MRI visualization, makes it a potential screening method for alert diagnosis of progressive ALI. On the other hand, *i.v.* administration of Neu@PFC provides a quantitative assessment of the extent of ALI due to the guidance of chemokine gradient in the bloodstream. Neu@PFC's infiltration in inflamed lungs after both *i.t.* and *i.v.* administration routes were further confirmed through IVM imaging, with subsequent ex vivo validation by histological and confocal analysis of

lung tissue. Besides, Neu@PFC exhibited good biocompatibility and minimal systemic side effects. Taken together, the successful development of Neu@PFC for precise ^{19}F-MRI diagnosis of ALI presents a smart living-cell-based delivery strategy of contrast agents and contributes toward a deep understanding of the physiological progression of ALI.

Although the neutrophil-based ^{19}F-MRI imaging assay has shown interesting results in ALI diagnosis, the direct use of neutrophils as probe carriers is constrained by their limited source and short lifespan. Larger studies are necessary to affirm the safety and clinical efficacy of the assay. Besides, the complex interplay among neutrophil subtypes and their dichotomous roles in disease progression introduces additional complexity, as administered living neutrophils might be prone to reprogramming in the absence of stringent control measures. Given their roles in both inflammation and repair, it is crucial to maintain a balance between the harmful and beneficial functions of neutrophils. Concerns regarding off-target effects are also pertinent in the context of neutrophil-based probe delivery. Unwanted probe release might occur at the sites of aged neutrophils clearance areas such as the liver, spleen, and bone marrow, or the places with acute or chronic inflammation. Despite these hurdles, neutrophil-based live-cell probes hold significant promise for advancing the management of inflammatory diseases.

Supporting Information

Supporting Information is available from the Wiley Online Library or from the author.

Acknowledgements

S.L. and L.Z. contributed equally to this work. This work was supported by the National Key Research and Development Program of China (2018YFA0704000), the National Natural Science Foundation of China (U21A20392, 82127802, 21921004, 22404064), the Hubei Provincial Natural Science Foundation of China (grant no. 2023BCB092), CAS Youth Interdisciplinary Team (JCTD-2022-13). X.Z. acknowledges the support from the Tencent Foundation through the XPLORER PRIZE, and S.C. acknowledges the support from the Young Top-notch Talent Cultivation Program of Hubei Province.

Conflict of Interest

The authors declare no conflict of interest.

Data Availability Statement

The data that support the findings of this study are available from the corresponding author upon reasonable request.

Keywords

^{19}F-MRI, acute lung injury, diagnosis, nanoengineered neutrophil, perfluorocarbon

Received: January 29, 2024
Revised: August 26, 2024
Published online: October 3, 2024

[1] A. P. Wheeler, G. R. Bernard, *Lancet* **2007**, *369*, 1553.
[2] N. T. Mowery, W. T. H. Terzian, A. C. Nelson, *Curr. Probl. Surg.* **2020**, *57*, 100777.
[3] H. D. Yue, C. Gao, J. Y. Li, H. B. Chen, S. M. Y. Lee, R. F. Luo, R. B. Wang, *Adv. Mater.* **2023**, *35*, 2211626.
[4] E. Fan, D. Brodie, A. S. Slutsky, *Jama-J. Am. Med. Assoc.* **2018**, *319*, 698.
[5] E. R. Johnson, M. A. Matthay, *J. Aerosol. Med. Pulm. Drug Deliv.* **2010**, *23*, 243.
[6] C. M. Wu, X. Y. Chen, Y. P. Cai, J. A. Xia, X. Zhou, S. Xu, H. P. Huang, L. Zhang, X. Zhou, C. L. Du, Y. Y. Zhang, J. Song, S. J. Wang, Y. C. Chao, Z. Y. Yang, J. Xu, X. Zhou, D. C. Chen, W. N. Xiong, L. Xu, F. Zhou, J. J. Jiang, C. X. Bai, J. H. Zheng, Y. L. Song, *Jama Intern. Med.* **2020**, *180*, 934.
[7] F. Y. Shen, Z. J. Xiong, Y. M. Wu, R. Peng, Y. Wang, L. L. Sun, C. H. Fan, Z. Liu, *Angew. Chem., Int. Ed.* **2023**, *62*, 202301147.
[8] S. M. Fernando, B. L. Ferreyro, M. Urner, L. Munshi, E. Fan, *Can. Med. Assoc. J.* **2021**, *193*, E761.
[9] M. Zompatori, F. Ciccarese, L. Fasano, *Eur. Respir. Rev.* **2014**, *23*, 519.
[10] E. T. Obadina, J. M. Torrealba, J. P. Kanne, *Br. J. Radiol.* **2013**, *86*, 20120614.
[11] K. M. Marquis, M. M. Hammer, K. Steinbrecher, T. S. Henry, C. Y. Lin, A. Shifren, C. A. Raptis, *Radiographics* **2023**, *43*, 220176.
[12] B. M. Elicker, K. T. Jones, D. M. Naeger, J. A. Frank, *Radiol. Clin. North Am.* **2016**, *54*, 1119.
[13] C. Giraudo, L. Evangelista, A. S. Fraia, A. Lupi, E. Quaia, D. Cecchin, M. Casali, *Int. J. Mol. Sci.* **2020**, *21*, 894.
[14] H. U. Kauczor, A. Hanke, E. J. R. van Beek, *Eur. Radiol.* **2002**, *12*, 1962.
[15] E. A. Akam, E. Abston, N. J. Rotile, H. R. Slattery, I. Y. Zhou, M. Lanuti, P. Caravan, *Chem. Sci.* **2020**, *11*, 224.
[16] H. D. Li, X. C. Zhao, Y. J. Wang, X. Lou, S. Z. Chen, H. Deng, L. Shi, J. S. Xie, D. Z. Tang, J. P. Zhao, L.-S. Bouchard, L. M. Xia, X. Zhou, *Sci. Adv.* **2021**, *7*, eabc8180.
[17] S. Z. Chen, L. Xiao, Y. Li, M. S. Qiu, Y. P. Yuan, R. Zhou, C. G. Li, L. Zhang, Z. X. Jiang, M. L. Liu, X. Zhou, *Angew. Chem., Int. Ed.* **2022**, *61*, 202213495.
[18] H. Y. Lin, X. X. Tang, A. Li, J. H. Gao, *Adv. Mater.* **2021**, *33*, 2005657.
[19] P. Bouvain, Z. Ding, S. Kadir, P. Kleimann, N. Kluge, Z.-B. Tiren, B. Steckel, V. Flocke, R. Zalfen, P. Petzsch, T. Wachtmeister, G. John, N. Subramaniam, W. Krämer, T. Strasdeit, M. Mehrabipour, J. M. Moll, R. Schubert, M. R. Ahmadian, F. Bönner, U. Boeken, R. Westenfeld, D. R. Engel, M. Kelm, J. Schrader, K. Köhrer, M. Grandoch, S. Temme, U. Flögel, *Nat. Cardiovasc. Res.* **2023**, *2*, 126.
[20] P. Bouvain, S. Temme, U. Flögel, *Wiley Interdiscip. Rev. Nanomed. Nanobiotechnol.* **2020**, *12*, e1639.
[21] O. S. Pavlova, M. V. Gulyaev, L. L. Gervits, A. A. Hurshkainen, A. V. Nikulin, V. M. Puchnin, E. D. Teploukhova, T. A. Kuropatkina, N. V. Anisimov, N. A. Medvedeva, Y. A. Pirogov, *Magn. Reson. Med.* **2023**, *89*, 2318.
[22] S. Li, W. P. Jiang, Y. P. Yuan, M. J. Sui, Y. Q. Yang, L. Q. Huang, L. Jiang, M. L. Liu, S. Z. Chen, X. Zhou, *ACS Appl. Mater. Interfaces* **2020**, *12*, 57290.
[23] Y. G. Sun, J. Yang, Y. B. Li, J. Luo, J. M. Sun, D. S. Li, Y. C. Wang, K. Wang, L. L. Yang, L. A. Wu, X. L. Sun, *Mol. Cancer* **2022**, *21*, 212.
[24] U. Flögel, S. Temme, C. Jacoby, T. Oerther, P. Keul, V. Flocke, X. W. Wang, F. Bönner, F. Nienhaus, K. Peter, J. Schrader, M. Grandoch, M. Kelm, B. Levkau, *Nat. Commun.* **2021**, *12*, 5847.
[25] M. Modo, H. Ghuman, R. Azar, R. Krafty, S. F. Badylak, T. K. Hitchens, *Biomaterials* **2022**, *282*, 121386.
[26] H. B. Wang, X. N. Li, J. Wang, J. N. Wang, H. Y. Zou, X. S. Hu, L. Q. Yang, P. H. Shen, R. A. K. Q. Wang, Y. B. Li, K. Wang, L. L. Yang, L. N. Wu, X. L. Sun, *Nano Lett.* **2023**, *23*, 2964.
[27] Y. X. Chen, D. T. Qin, J. H. Zou, X. B. Li, X. D. Guo, Y. Tang, C. Liu, W. Chen, N. Kong, C. Y. Zhang, W. Tao, *Adv. Mater.* **2023**, *35*, 2207787.

[28] G. K. Aulakh, *Cell Tissue Res.* **2018**, *371*, 577.
[29] A. Margraf, C. A. Lowell, A. Zarbock, *Blood* **2022**, *139*, 2130.
[30] J. W. Xue, Z. K. Zhao, L. Zhang, L. J. Xue, S. Y. Shen, Y. J. Wen, Z. Y. Wei, L. Wang, L. Y. Kong, H. B. Sun, Q. N. Ping, R. Mo, C. Zhang, *Nat. Nanotechnol.* **2017**, *12*, 692.
[31] J. S. Huang, P. H. Cheng, C. Xu, S. S. Liew, S. S. He, Y. Zhang, K. Y. Pu, *Angew. Chem., Int. Ed.* **2022**, *61*, 202203235.
[32] P. Zhang, Q. Zhao, M. S. Shi, C. C. Yin, Z. F. Zhao, K. L. Shen, Y. Qiu, Y. Xiao, Y. B. Zhao, X. L. Yang, Y. F. Zhang, *Nano Lett.* **2020**, *20*, 261.
[33] X. G. Liu, Y. K. Duan, D. H. Hu, M. Wu, C. J. Chen, P. B. Ghode, G. Magarajah, N. Thakor, X. Liu, C. B. Liu, Z. H. Sheng, H. R. Zheng, B. Liu, *ACS Mater. Lett.* **2021**, *3*, 1284.
[34] J. Y. Che, A. Najer, A. K. Blakney, P. F. McKay, M. Bellahcene, C. W. Winter, A. Sintou, J. Q. Tang, T. J. Keane, M. D. Schneider, R. J. Shattock, S. Sattler, M. M. Stevens, *Adv. Mater.* **2020**, *32*, 2003598.
[35] L. Sun, J. E. Zhou, T. S. Luo, J. Wang, L. Q. Kang, Y. Y. Wang, S. G. Luo, Z. H. Wang, Z. Y. Zhou, J. X. Zhu, J. H. Yu, L. Yu, Z. Q. Yan, *Adv. Mater.* **2022**, *34*, 2109969.
[36] B. Li, J. Z. Yang, Q. Huang, Y. Zhang, C. Peng, Y. J. Zhang, Y. He, J. Y. Shi, W. X. Li, J. Hu, C. H. Fan, *NPG Asia Mater* **2013**, *5*, e44.
[37] V. Forest, J. Pourchez, *Adv. Drug. Deliver. Rev.* **2022**, *183*, 114173.
[38] R. Holman, O. Lorton, P. C. Guillemin, S. Desgranges, C. Contino-Pepin, R. Salomir, *Front. Chem.* **2022**, *9*, 810029.
[39] M. X. Hao, L. L. Zhu, S. Y. Hou, S. J. Chen, X. Q. Li, K. M. Li, N. C. Zhu, S. S. Chen, L. J. Xue, C. Y. Ju, C. Zhang, *ACS Nano* **2023**, *17*, 1663.
[40] B. Ebner, P. Behm, C. Jacoby, S. Burghoff, B. A. French, J. Schrader, U. Flögel, *Circ. Cardiovasc. Imaging* **2010**, *3*, 202.